Multiscale finite element modelling of ductile damage behaviour of the human femur under dynamic loading

Hakim Naceur, Jamila Rahmoun, Julien Halgrin, Patrick Chabrand

Multiscale finite element modelling of ductile damage behaviour of the human femur under dynamic loading

H Naceur[1], J Rahmoun[1], J Halgrin[2] and P Chabrand[2]

Abstract

In this paper, we propose a new multiscale finite element methodology based on a recently developed micromechanical damage model for the modelling of the human bone behaviour under dynamic loading. The damage is carried out by the framework of the limit analysis based on the MCK (Monchiet, Charkaluk and Kondo) criterion. We first present the methodology allowing the estimation of elastic anisotropic properties of porous media by means of Mori–Tanaka homogenisation scheme. Then, we develop the formulation of the integrated yield criterion derived by considering trial velocity field inspired from the Eshelby inhomogeneous inclusion solution. The obtained micromechanical model is implemented via a User Material routine within the explicit dynamic code LS-DYNA©. The proposed micromechanical model has been applied successfully for the estimation of the mechanical properties of a human proximal femur under dynamic loading. From the obtained numerical results, it has been shown that the present model has improved the strength prediction of osteoporotic femurs by representing the failure risk in a more realistic approach.

Keywords

Ductile damage, micromechanics, multiscale homogenisation, solid-shell finite element, cancellous bone

Introduction

Osteoporotic hip fractures represent a burden of mortality on the growing population of old patients. To estimate hip fracture and plan the preventive intervention, the strength of the proximal femur must be precisely quantified. However, a method that would evaluate complete bone strength is not yet established. The amount of bone tissue obtained by measuring bone mineral density by

[1]Lab. LAMIH, Université de Valenciennes, Valenciennes, France

[2]Institut des Sciences du Mouvement, Université de la Méditerranée, Marseille, France

Corresponding author:

H Naceur, Lab. LAMIH, UMR 8201 CNRS, Université de Valenciennes, 59313 Valenciennes, France.

Email: hakim.naceur@univ-valenciennes.fr

dual X-ray absorptiometry, has long been considered as a surrogate marker of bone strength (Cummings and Melton, 2002; Marshall et al., 1996; Siri et al., 2004). Consequently, this technique remains unable to estimate bone quality, which is intrinsically a mechanical property depending on properties such as porosity and microstructural anisotropy.

The structural capacity of the femur may also be affected by other factors independent of the density; we can find in the literature numerous references dealing with the influential factors on the bone strength of the proximal femur. For instance, let us cite the work of Lotz and Hayes (1990) who determined the loads and energies needed to cause a proximal femur fracture and proved the correlations between the fracture load and bone density measured by quantitative computed tomography (CT). Courtney et al. (1995) compared the loads at fracture of the proximal femur from the cadavers of older and younger individuals and found a 20% increase in failure load due to the high strain rate (Courtney et al., 1994). Cristofolini et al. (2009) studied the strain distribution of 12 pairs of human femurs, using six loading configurations to cover the range of directions spanned by the hip joint force. The influence of loading direction on the fracture load of the elderly proximal femur was investigated by Pinilla et al. (1996). In particular, Ford et al. (1996) reported a study on the structural capacity of the proximal femur in four loading configurations that represent a range of possible falls on the greater trochanter. Following these studies, it was concluded that, there exist a direction of loading in which a fracture easily occurs, and the loading direction influences the generation of a proximal femur fracture. However, there was a lack in the previous studies regarding the use of subjects for whom the presence of osteoporosis was not evaluated. Among recent works, Lenaerts and van Lenthe (2009) carried out a multilevel modelling of the proximal human femur in order to quantify the effect of osteoporosis. They concluded that geometry-based as well as voxel-based Finite Element (FE) models can provide good predictions of femoral bone strength, especially when the models are tuned to specific loading scenarios. They stated at the end of their investigation that the precise failure mechanisms and associated material properties are still not well understood. In their very interesting investigation, Christen et al. (2010) presented a survey of the current state of the art for multiscale modelling and assessed its potential to better predict an individual's risk of fracture in a clinical setting. They concluded that multiscale approach to modelling the mechanics of bone allows a more accurate characterisation of bone fracture behaviour and such models could also include the effects of ageing, osteoporosis and drug treatment. Therefore, it is necessary to develop a noninvasive method for accurate quantitative structural analysis that combines information on both morphology and bone density in a three-dimensional (3D) distribution.

CT-based FE analysis which incorporates information on both 3D architecture and bone density distribution, could possibly achieve precise assessment of the strength of the proximal femur (Cody et al., 1999). Former studies on CT-based FE analysis of bone strength have shown to produce an estimate of the failure load of the proximal femur with reasonable accuracy for given boundary conditions (Bessho et al., 2007; Keyak, 2001; Koivumäki et al., 2012). Unfortunately, the resulting voxel-based FE models require high volumes of data and the computational costs become quickly very high, which makes them useless in the practice.

Due to the multiscale nature of the bone, there have been several theoretical developments to obtain reasonable estimates of the micro- and macroscopic mechanical behaviours within the context of mechanics of heterogeneous media (Cristofolini et al., 2008). Homogenisation techniques have been then developed, to model the elastoplastic and the fracture behaviours of the femoral bone (Aoubiza et al., 1996; Arnoux et al., 2002; Cristofolini et al., 2008). Furthermore, micromechanical approaches coupled with CT-based FE models were revealed to be more appropriate when the robustness of computation and accuracy of results are of interest (Cristofolini et al., 2008).

The predictive potential of the so-called micromechanical formulations has been established using physically and statistically independent sets of experiments.

It is well established in the FE analysis, that 8-node hexahedral elements are preferred since their convergence rate is sensibly higher than the 4-node tetrahedral elements. This may allow the use of 8-node hexahedral element volume mesh with a moderate mesh density to model the complexity of anatomical geometry. Nowadays, despite the fact that generating a 3D hex mesh, still requiring extensive manual meshing operations, the resulting FE model offers significant benefits compared to a classical tetrahedral mesh (solution accuracy and regularity, angle distribution, better contact treatment and also a globally better convergence rate). When comparing linear hexahedral and tetrahedral elements, it has been proven that hex-elements give better quality results in many structural applications (Cifuentes and Kalbag, 1992), including nonlinear elastoplastic analysis (Benzley et al., 1995). Schonning et al. (2009) have developed a standard hexahedral FE model of the human femur accounting for the material characteristics of cortical bone, cancellous bone and bone marrow.

In damage mechanics, there exist principally two modelling approaches which have been extensively used in the last two decades to study the ductile damage and its influence on the material behaviour. The first approach was pioneered by Gurson (1977), it is based on the void nucleation, growth and coalescence. It uses the void volume fraction (porosity) as a 'scalar' damage variable in the plastic potential in order to model the damage effects (Nedoushan et al., 2013; Li et al., 2013). The second approach treats the damage effect on the overall elastoplastic behaviour of the material. The Continuum Damage Mechanics (Saanouni and César de Sa, 2011; Chaboche, 2013) uses a scalar damage variable to represent the ductile defect on the other thermomechanical fields. This kind of Continuum Damage Mechanics-based phenomenological approach has been extensively applied to numerous metal forming processes (Saanouni and César de Sa, 2011; Niazi et al., 2012).

In this paper, we propose a micromechanical ductile damage model of the human femur bone behaviour in view of an integration of bone damage for the simulation of necking and rupture initiation. The determination of elastic properties has been made by using the Mori–Tanaka scheme (Mori and Tanaka, 1973) and experimental measurements of anisotropy by microtomography techniques (Christen et al., 2010; Cristofolini et al., 2008; Lenaerts and van Lenthe, 2009). The nonlinear behaviour is taken into account by a coupling between plasticity and damage on a microscopic scale. The damage has been carried out by using a limit analysis approach based on the MCK criterion (Monchiet et al., 2011). The derived yield function is deduced by the consideration of new trial velocity fields inspired from the Eshelby (Liu, 2010) exterior point solution to inclusions problem in which the eigen-strains are unknown. The obtained ductile damage behaviour law is implemented via a user material routine UMAT within the explicit dynamic commercial code $LS-DYNA©$ (Livermore Software Technology Corporation, 2007) for the prediction of the global response of the femur.

At the macro-level, we propose an original hex-shell FE element model to capture the mechanical response of the femur. The hex-shell elements (called also Solid-Shell elements) are a variety of FE models midway between 3D solid elements and thin shells (Harnau and Schweizerhof, 2002; Naceur et al., 2013). They offer many advantages compared to classical solid elements, because of their kinematics simplicity, their ability in modelling complex biological structures generally composed of bulk and thin-walled regions. In the proposed FE model, different locking phenomena have been resolved using the Assumed Natural Strain (ANS) method and the Enhanced Assumed Thickness Strain where a seventh enrichment variable is suppressed by static condensation. Finally, we present some applications in biological tissues to estimate the local mechanical properties of the femoral head and the global response of the human femur under compression test.

Formulation of the micromechanics-based ductile damage model of the femur bone

Homogenisation scheme for the elastic anisotropic bone behaviour

In this section, we briefly recall the common backgrounds of homogenisation methods for random heterogeneous materials, which will be used for the formulation of micromechanical model for the human femur bone.

Description of the representative elementary volume. Micromechanical analysis provides links between macroscopic properties of the material and its microstructure. In common homogenisation methods (Chaboche, 2013), the material is understood as a macro-homogeneous, but microheterogeneous body filling a representative elementary volume (REV). The main task is to find the homogeneous material properties at macroscopic scale based on the available information at the microscopic scale. In general, the microstructure within one REV is so complicated that it cannot be described in complete detail. Therefore, quasi-homogeneous subdomains with known physical quantities (such as volume fraction or elastic properties) are generally privileged; they are called material phases.

The *homogenised* mechanical behaviour of the overall material, i.e. the relation between homogeneous deformations acting on the boundary of the REV and the resulting (averaged) stresses can then be estimated from the mechanical behaviour of the aforementioned homogeneous phases (representing the inhomogeneities), their dosages, their geometrical shapes and interactions.

In the present study, the femoral bone can be considered as a multiscale heterogeneous material with a matrix phase weakened by micropores and which exhibits transversely isotropic symmetry. The REV of both cortical and trabecular bone is composed of an isotropic linear elastic solid matrix with the stiffness tensor $\mathbb{C}^{(m)}$ and of a random distribution of ellipsoidal shaped voids made of phases r ($r = 1, \ldots, N$) with the elasticity tensor $\mathbb{C}^{(r)}$. Under the isotropic assumption of the solid matrix, the stiffness tensor; $\mathbb{C}^{(m)}$, reads $\mathbb{C}^{(m)} = 3\kappa^{(m)}\mathbb{J} + 2\mu^{(m)}\mathbb{K}$, where $\kappa^{(m)}$ and $\mu^{(m)}$ represent the bulk and shear moduli of the matrix, respectively. $\mathbb{J}$ and $\mathbb{K}$ are the isotropic fourth order tensor projectors having minor and major symmetries. The inclusions of the phase r are taken to be identical in shape and orientation with normal $\underline{n}$, radius a and the average half-opening c.

Determination of effective elastic properties. Let $\boldsymbol{E}$ be the uniform macroscopic strain field prescribed on the boundary of the REV (see Figure 1). The corresponding displacement $\underline{u}(x)$ boundary condition reads

$$\underline{u}(x) = \boldsymbol{E} \cdot \underline{x} \quad \forall x \epsilon \partial\Omega \tag{1}$$

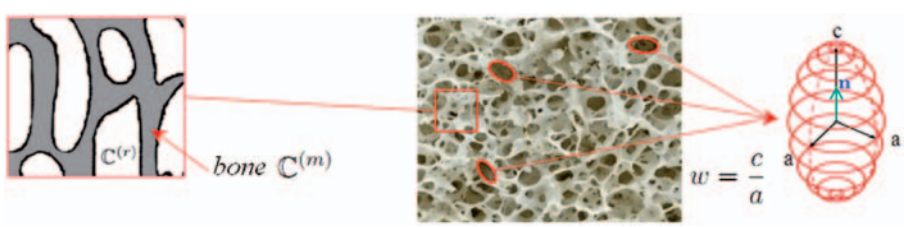

Figure 1. Description of the representative elementary volume.

This implies the following average rule between the strains at microscopic and macroscopic scales in Ω

$$< \boldsymbol{\varepsilon} >_{\Omega} = \boldsymbol{E} \tag{2}$$

$< . >_{\Omega}$ denotes the volumetric average on Ω. Assuming now a linear elastic behaviour for each phase within the REV, the constitutive relation is given in the form $\boldsymbol{\sigma}(x) = \mathbb{C}(x) : \boldsymbol{\varepsilon}(x), \quad \forall x \in \Omega$. Accordingly, a fourth-order concentration tensor $\mathbb{A}(x)$, relating the microscopic strain $\boldsymbol{\varepsilon}(x)$ to the macroscopic strain $\boldsymbol{E}$, is introduced in the classical form

$$\boldsymbol{\varepsilon}(x) = \mathbb{A}(x) : \boldsymbol{E} \tag{3}$$

The strain average rule in equation (2) implies $< \mathbb{A}(x) >_{\Omega} = \mathbb{I}$ where $\mathbb{I}$ is the fourth-order symmetric identity tensor. Taking the average of the microscopic stress $\boldsymbol{\sigma}(x)$ and using equation (3), the macroscopic elastic behaviour of material can be expressed in the form $\boldsymbol{\Sigma} = \mathbb{C}^{hom} : \boldsymbol{E}$, with

$$\mathbb{C}^{hom} = < \mathbb{C}(x) : \mathbb{A}(x) >_{\Omega} \tag{4}$$

Based on matrix-inclusion problems (Liu, 2010) and the Mori–Tanaka scheme (Mori and Tanaka, 1973) which commonly deals with inclusions interaction in composite materials, we assume a constant localisation tensor by phase. Therefore, by using the identity $< \mathbb{A} >_{\Omega} = \mathbb{I}$ in equation (4), an estimate for the homogenised elastic stiffness tensor of the bone material can be obtained as (Rahmoun et al., 2009)

$$\mathbb{C}^{hom} = \mathbb{C}^{(m)} + \sum_{r=1}^{N} f^{(r)} (\mathbb{C}^{(r)} - \mathbb{C}^{(m)}) : \mathbb{A}_w^{(r)} : (f^{(m)} \mathbb{I} + \sum_{s=1}^{N} f^{(s)} \mathbb{A}_w^{(s)})^{-1} \tag{5}$$

where $f^{(m)}$ and $f^{(r)}$ are the volume fraction of matrix and inclusions, respectively and where the two sums are taken over all phases of the heterogeneous material in the REV. $\mathbb{A}_w^{(r)}$ denotes the strain concentration tensor associated with the r-th phase family of inclusions of aspect ratio w, which writes

$$\mathbb{A}_w^{(r)} = [\mathbb{I} + \mathbb{P}_w^{(r)} : \left(\mathbb{C}^{(r)} - \mathbb{C}^{(m)}\right)]^{-1} \tag{6}$$

$\mathbb{P}_w^{(r)}$ is the fourth-order Hill polarisation tensor (Chaboche, 2013) which depends on the shape and the orientation of the r-th family of inclusions $\mathbb{C}^{(r)}$ (considered here as spheroid) and the elastic stiffness of the reference medium $\mathbb{C}^{(m)}$. The necessary detail can be found in Rahmoun et al., 2009, and only a summary of the main results of the model will be presented here.

Application to the trabecular bone effective properties

We aim now to investigate the effect of structural anisotropy of the femoral bone. One approach for the modelling of bone microstructural architecture can be derived thanks to the fabric tensor. Thus, as in a previous work by the authors (Rahmoun et al., 2009), the formalism of the stiffness tensor

given by equation (5) can be coupled with experimental measurements of the architectural anisotropy obtained from X-ray microtomography and the Mean Intercept Length (MIL) method (Christen et al., 2010; Cristofolini et al., 2008; Lenaerts and van Lenthe, 2009), which will be adopted to estimate the volume fractions of pores.

Following a methodology used by Voyiadjis et al. (2007) for orthotropic materials, the 3D anisotropy can be determined by measuring the MIL in three mutually perpendicular planes (see Figure 2) and recognising the result as a second rank tensor $\boldsymbol{H}$ defining an ellipsoid.

Then, in the direction $\underline{n} = (\theta, \phi)$ (with $\theta \epsilon [0, \pi]$ and $\phi \epsilon [0, 2\pi]$), the mean length of pores can be obtained by

$$\bar{l}(\underline{n}) = 2c = \frac{1}{\sqrt{\underline{n} \otimes \underline{n} : \boldsymbol{H}}} \tag{7}$$

It is convenient to express the volume of the ellipsoidal inclusion r in the direction $\underline{n}$ as

$$V^{(r)} = \frac{4}{3}\pi a^2 \frac{\bar{l}(\underline{n})}{2} \tag{8}$$

Thus, by using equation (7), the average volume of voids can be obtained analytically

$$V_p = \frac{1}{4\pi}\int_0^{2\pi}\int_0^{\pi} \frac{4\pi}{3}\frac{\bar{l}(\theta,\phi)}{2}\frac{\bar{l}^2(\theta+\pi/2,\phi)}{4}\sin\theta\Big)\mathrm{d}\theta\mathrm{d}\phi = \frac{\pi}{6}\frac{\arccos(\lambda_3/\lambda_1)}{\left(\lambda_1^2-\lambda_3^2\right)^{1/2}}\lambda_3^{-1/2} \tag{9}$$

where λ_i are the eigen values of the fabric tensor $\boldsymbol{H}$ and V the volume of the composite. Finally, the volume fraction of pores can be expressed as

$$f_p = N_p V_p \tag{10}$$

with N_p denotes the pores density (number of pores per unit volume). Let us notice that this expression of volume fraction of voids takes into account the orientation of pores distribution. Therefore, the effective stiffness equation (5) of the porous biological material takes the final form

$$\mathbb{C}^{hom} = \mathbb{C}^{(m)} + f_p\left(\mathbb{C}^{(p)} - \mathbb{C}^{(m)}\right) : \mathbb{A}_p : \left(f^{(m)}\mathbb{I} + f_p\mathbb{A}_p\right)^{-1} \tag{11}$$

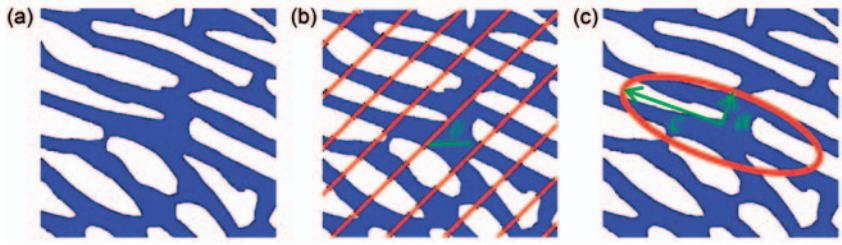

Figure 2. Fabric representation in 2D using Mean Intercept Length (MIL).

Micromechanical modelling of the nonlinear behaviour of bone

Constitutive plastic-damage model based on the MCK criterion. In this section, we present an extension of the micromechanical linear model for the case of nonlinear behaviour. The new model is based on a coupling between plasticity and damage on a microscopic scale. The damage has been carried out by using the framework of limit analysis of Gurson (1977) and its evolutions through the recent work of Monchiet et al. (2011), and Shen et al. (2011) called the MCK criterion.

In this approach, the studied domain is supposed to be composed of a spherical cavity of radius a subjected to a uniform eigen-strain rate $\boldsymbol{d}^*$ and embedded in a spherical cell with the radius b (Figure 3). The spherical frame (coordinates r, φ, θ) is considered to describe the studied cell.

The trial velocity field $\underline{v}$ in the matrix, required for the limit analysis of the hollow sphere, as stated by Gurson (1977), takes classically the following general form:

$$\underline{v} = \boldsymbol{A} \cdot \underline{x} + \underline{v}^E \tag{12}$$

in which $\boldsymbol{A}.\underline{x}$ is associated to a uniform strain rate $\boldsymbol{A}$ and $\underline{v}^E$ is a heterogeneous field which corresponds to the expansion of the cavity. The assumption of incompressible matrix induces $tr(\boldsymbol{A}) = 0$ and $div(\underline{v}^E) = 0$.

From the exterior point Eshelby solution (Liu, 2010), a more refined velocity field $\underline{v}^E$, in the particular case of a spherical inclusion, can be given by Shen et al. (2011)

$$\underline{v}^E = \sum_{r=1}^{r=6} \underline{v}^r \boldsymbol{d}_r^* \tag{13}$$

where $\boldsymbol{d}_r^*$ is related to the eigen-strain in the inhomogeneity $\boldsymbol{d}^*$. The microscopic plastic strain rate $\boldsymbol{d}$ derived from the velocity field equation (12) is defined by

$$\boldsymbol{d} = \boldsymbol{A} + \boldsymbol{d}^E \tag{14}$$

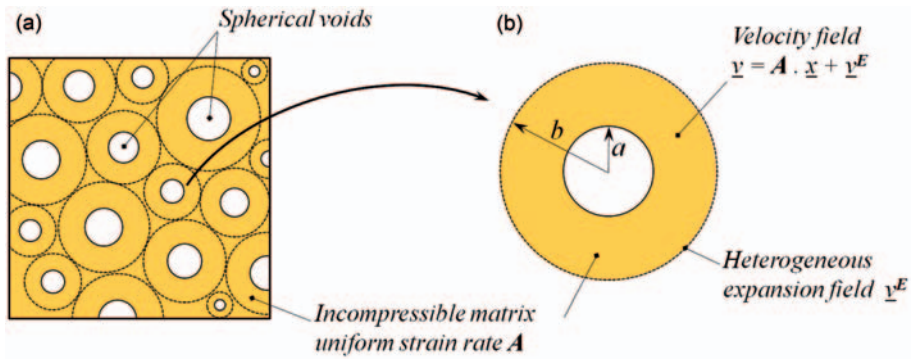

Figure 3. Micromechanical plastic-damage model assumptions: (a) Representative volume element of a porous medium. The spherical voids are distributed randomly. The solid spheres denote the voids, and the dashed spheres, their distribution and (b) Representation of a spherical unit cell of radius b, including a spherical void of radius a.

with $\boldsymbol{d}^E = \nabla_s \underline{v}^E$, the symmetric part of the velocity gradient associated to $\underline{v}^E$ Monchiet et al., 2011. The microscopic dissipation $\pi(\boldsymbol{d}) = d_0 d_{\text{eq}}$ where $d_{\text{eq}} = \sqrt{\frac{2}{3}\boldsymbol{d}' : \boldsymbol{d}'}$ is the equivalent plastic strain rate defined by (see Monchiet et al., 2011)

$$d_{\text{eq}}^2 = A_{\text{eq}}^2 + 2\sum_{r=1}^{r=6} d_r^*(\boldsymbol{A} : \boldsymbol{d}'^r) + \sum_{r=1}^{r=6}\sum_{s=1}^{s=6} d_r^* d_s^*(\boldsymbol{d}'^r : \boldsymbol{d}'^s) \tag{15}$$

and $\boldsymbol{d}'$ is the deviatoric part of strain tensor $\boldsymbol{d}$. Then, following the Hill–Mandel lemma, the macroscopic strain rate $\boldsymbol{D}$ is related to the local strain rate $\boldsymbol{d}$, by the average rule

$$\boldsymbol{D} = \frac{1}{|\Omega|}\int_{\Omega} \boldsymbol{d}\,\mathrm{d}V \tag{16}$$

where $|\Omega|$ is the volume of the studied cell (matrix + void).

The macroscopic plastic dissipation can be obtained through a minimisation procedure on the remaining unknown parameters $\boldsymbol{d}'^*$

$$\Pi(\boldsymbol{D}) = \min_{\boldsymbol{d}'^*} \tilde{\Pi}\left(\boldsymbol{D}, \boldsymbol{d}'^*\right) \quad \text{with} \quad \tilde{\Pi}\left(\boldsymbol{D}, \boldsymbol{d}'^*\right) = \frac{\sigma_y}{|\Omega|}\int_{\Omega-\omega} d_{\text{eq}}\,\mathrm{d}V \tag{17}$$

with ω denotes the volume of the void and σ_y the yield stress. The flow surface, related the macroscopic dissipation, is then assumed to be given by

$$\boldsymbol{\Sigma} = \frac{\partial \Pi}{\partial \boldsymbol{D}} \tag{18}$$

Finally, following the limit analysis method of Gurson (1977), the approximate expression of the macroscopic yield function is obtained as (Monchiet et al., 2011)

$$\Phi(\boldsymbol{\Sigma}, f) = \frac{\Sigma_{\text{eq}}^2}{\sigma_y^2} + 2f\cosh\left(\sqrt{\frac{9}{4}\frac{\Sigma_h^2}{\sigma_y^2} + \frac{2}{3}\frac{\Sigma_{\text{eq}}^2}{\sigma_y^2}}\right) - 1 - f^2 = 0 \tag{19}$$

where Σ_h denotes the hydrostatic stress, Σ_{eq} the macroscopic von-Mises equivalent stress and f the actual material porosity.

Numerical integration of the plastic-damage model. As stated before in our objectives, we aim to formulate and implement the MCK criterion (Monchiet et al., 2011), in order to study the femoral bone behaviour under dynamic loading. The implementation has been carried out within the explicit dynamic code LS – DYNA© via the user-routine UMAT (Livermore Software Technology Corporation, 2007).

At first an additional nonlinear hardening variable $\bar{\sigma}$ is introduced in the MCK criterion (equation (19)) representing the updated yield stress of the matrix

$$\Phi(\boldsymbol{\Sigma}, f, \bar{\sigma}) = \frac{\Sigma_{\text{eq}}^2}{\bar{\sigma}^2} + 2f\cosh\left(\sqrt{\frac{9}{4}\frac{\Sigma_h^2}{\bar{\sigma}^2} + \frac{2}{3}\frac{\Sigma_{\text{eq}}^2}{\bar{\sigma}^2}}\right) - 1 - f^2 \leq 0 \tag{20}$$

We introduce the macroscopic plastic flow rule obtained by upscaling, according to the normality rule

$$\boldsymbol{D}^p = \dot{\boldsymbol{E}}^p = \dot{\lambda}\frac{\partial \Phi}{\partial \boldsymbol{\Sigma}} \tag{21}$$

in which $\boldsymbol{D}^p$ is the macroscopic plastic strain rate and $\dot{\lambda}$ is a plastic multiplier. Taking into account the incompressibility of the matrix, the porosity evolution law which characterises the damage growth, reads

$$\dot{f} = \dot{f}_n + \dot{f}_g \tag{22}$$

in which $\dot{f}_n$ and $\dot{f}_g$ represent the rates of volume fraction increase of the microcavities due to nucleation and growth, respectively.

The rate of volume fraction increase due to nucleation $\dot{f}_n$ may be controlled using the equivalent plastic strain. In the case of a random distribution of inclusions, the increase rate of nucleation follows a Gaussian probability

$$\dot{f}_n = \frac{f_N}{s_N\sqrt{2\pi}}\exp\left\{-\frac{1}{2}\left(\frac{\bar{\varepsilon}^p - \varepsilon_N}{s_N}\right)^2\right\}\dot{\bar{\varepsilon}}^p \tag{23}$$

where $\bar{\varepsilon}^p$ is the actual equivalent plastic strain, ε_N is the mean normal distribution of the nucleation strain, s_N the standard deviation of the Gaussian normal distribution and f_N the volume fraction of nucleated voids.

The rate of volume fraction increase due to the growth of microcavities $\dot{f}_g$, derives from the plastic incompressibility of the matrix which is defined by

$$\dot{f}_g = 3(1-f)tr(\boldsymbol{D}^p) \tag{24}$$

Following Gurson (1977), the equivalent plastic strain rate of the matrix is derived using the assumption of incompressibility of the matrix. It is expressed by the equivalence between the plastic work dissipated by the material and the one dissipated by the matrix; it is expressed as

$$\dot{\bar{\varepsilon}}^p = \frac{1}{(1-f)\bar{\sigma}}\boldsymbol{\Sigma} : \boldsymbol{D}^p \tag{25}$$

Finally, coalescence phase of the microcavities is introduced using the Tvergaard and Needleman model (Oral et al., 2012) in order to consider the effect of void coalescence f_c in the numerical implementation

$$f^* = \begin{cases} f & \text{if} \quad f \le f_c \\ f_c + \alpha(f - f_c) & \text{if} \quad f > f_c \end{cases} \tag{26}$$

where f_c represents the porosity at the onset of coalescence and $\alpha = (f_U - f_c)/(f_F - f_c)$ is a factor describing the acceleration of the material degradation during coalescence, as shown in Figure 4. f_F and f_U represent the porosity and the value of f^* at failure, respectively.

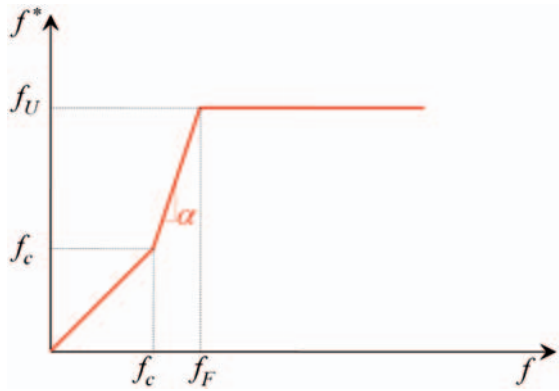

Figure 4. Evolution of porosity model Oral et al. (2012).

The stress increment calculation between time steps t_n and t_{n+1} is carried out using the radial return mapping algorithm, including two stages.

At the beginning, a trial stress $\boldsymbol{\Sigma}^{\text{trial}} = \boldsymbol{\Sigma}_n + \Delta\boldsymbol{\Sigma}^{\text{trial}}$ is estimated based on an elastic prediction using the strain increment $\Delta\boldsymbol{E}$ between the two time steps t_n and t_{n+1}

$$\Delta\boldsymbol{\Sigma} = \mathbb{C}^{\text{hom}} : \Delta\boldsymbol{E}^e = \mathbb{C}^{\text{hom}} : (\Delta\boldsymbol{E} - \Delta\boldsymbol{E}^p) = \Delta\boldsymbol{\Sigma}^{\text{trial}} - \mathbb{C}^{\text{hom}} : \Delta\boldsymbol{E}^p \tag{27}$$

where $\mathbb{C}^{\text{hom}}$ was determined by equation (11) and $\Delta\boldsymbol{\Sigma}^{\text{trial}}$ is the elastic trial stress increment.

The second stage consists in a plastic correction of the stress increment. First a projection direction $\partial\Phi/\partial\boldsymbol{\Sigma}^{\text{trial}}$ is evaluated using equation (20) together with and equation (21), which gives the following expressions for the deviatoric plastic strain increment $\Delta\boldsymbol{E}^{p\prime}$ and the hydrostatic plastic strain increment ΔE_h^p

$$\begin{cases} \Delta\boldsymbol{E}^{p\prime} &= \Delta\lambda\left(\dfrac{3}{\bar{\sigma}^2} + \dfrac{2f\sin\ \mathrm{h}\mathcal{R}}{\bar{\sigma}^2}\dfrac{}{\mathcal{R}}\right)\boldsymbol{\Sigma}^{\text{trial}\prime} \\ \Delta E_h^p &= \Delta\lambda\left(\dfrac{3f}{2\bar{\sigma}^2}\dfrac{\sin\ \mathrm{h}\mathcal{R}}{\mathcal{R}}\right)\Sigma_h^{\text{trial}} \end{cases} \tag{28}$$

with $\mathcal{R}^2 = \frac{9}{4}\left(\frac{\Sigma_h^{\text{trial}}}{\bar{\sigma}}\right)^2 + \frac{2}{3}\left(\frac{\Sigma_{\text{eq}}^{\text{trial}}}{\bar{\sigma}}\right)^2$

Now using equation (28) and with the definition of the macroscopic equivalent plastic strain increment $\Delta E_{\text{eq}}^p = \sqrt{2/3\Delta\boldsymbol{E}^{p\prime} : \Delta\boldsymbol{E}^{p\prime}}$, the following expression of the plastic multiplier increment $\Delta\lambda$ is obtained

$$\Delta\lambda = \frac{\bar{\sigma}^2}{\Sigma_{\text{eq}}^{\text{trial}}}\left(\frac{3\mathcal{R}}{6\mathcal{R} + 4f\sin\ \mathrm{h}\mathcal{R}}\right)\Delta E_{\text{eq}}^p \tag{29}$$

with $\Sigma_{\text{eq}}^{\text{trial}} = \left(2/3\boldsymbol{\Sigma}^{\text{trial}\prime} : \boldsymbol{\Sigma}^{\text{trial}\prime}\right)^{1/2}$

By considering the plastic consistency condition, $\dot{\Phi} = 0$, with the use of equation (20) and equation (29), one can obtain the final expression of the plastic multiplier $\Delta\lambda$

$$\Delta\lambda = \frac{\bar{\sigma}^2}{\gamma \Sigma_{\text{eq}}^{\text{trial}}} \left(\frac{3\mathcal{R}}{6\mathcal{R} + 4f \sin\ \text{h}\mathcal{R}} \right) \boldsymbol{g} : \mathbb{C}^{\text{hom}} : \Delta \boldsymbol{E} \tag{30}$$

with $\boldsymbol{g} = \partial\Phi/\partial\boldsymbol{\Sigma}^{\text{trial}}$ the stress projection direction, $\gamma = \boldsymbol{g} : \mathbb{C}^{\text{hom}} : \boldsymbol{g} - 2c(1-f)(\cos\ \text{h}\mathcal{R} - f) - E^T \partial\Phi/\partial\bar{\sigma}$, $E^T = \partial\bar{\sigma}/\partial\overline{\varepsilon^p}$ the hardening tangent elastoplastic modulus and $c = \partial\Phi/\partial\Sigma_{11} + \partial\Phi/\partial\Sigma_{22} + \partial\Phi/\partial\Sigma_{33}$.

Finally, the plastic strain increment is obtained using the integrated normality law given by equation (21). The last step is the computation of the consistent tangent elastoplastic tensor $\mathbb{C}^{\text{cons}}$ (defined by $\Delta\boldsymbol{\Sigma} = \mathbb{C}^{\text{cons}} : \Delta\boldsymbol{E}$) which is required to ensure the global convergence. The last can be achieved starting from equation (27) together with the expression of the plastic strain correction $\Delta\boldsymbol{E}^p$ we have

$$\Delta\boldsymbol{\Sigma} = \mathbb{C}^{\text{hom}} : \left(\Delta\boldsymbol{E} - \Delta\lambda \frac{\partial\Phi}{\partial\boldsymbol{\Sigma}} \right) = \mathbb{C}^{\text{cons}} : \Delta\boldsymbol{E} \tag{31}$$

with

$$\mathbb{C}^{\text{cons}} = \mathbb{C}^{\text{hom}} : \left[\mathbb{I} - \frac{\bar{\sigma}^2}{\gamma \Sigma_{\text{eq}}^{\text{trial}}} \left(\frac{3\mathcal{R}}{6\mathcal{R} + 4f \sin\ \text{h}\mathcal{R}} \right) \boldsymbol{g} \otimes \boldsymbol{g} : \mathbb{C}^{\text{hom}} \right] \tag{32}$$

Multiscale finite element formulation using an 8-node hex-shell element

Explicit time integration

For global numerical resolution, the central difference time integration method is used as proposed in Livermore Software Technology Corporation (2007). In the following, the governing equations are recalled briefly. For the current time step t_n, the accelerations are evaluated as

$$\underline{\ddot{u}}_n = \mathbf{M}^{-1} \left(\underline{P}_n - \underline{F}_n + \underline{H}_n \right) \tag{33}$$

where $\mathbf{M}$ is the diagonal mass matrix, $\underline{P}_n$ accounts for external and body force loads, $\underline{F}_n$ is the internal force vector and $\underline{H}_n$ is the hourglass stabilisation vector. Updating solution from time t_n to t_{n+1}, using the central difference time integration leads to

$$\underline{\dot{u}}_{n+1/2} = \underline{\dot{u}}_{n-1/2} + \Delta t^n\ \underline{\ddot{u}}_n \tag{34}$$

which gives the following displacement field

$$\underline{u}_{n+1} = \underline{u}_n + \Delta t_{n+1/2} \underline{\dot{u}}_{n+1/2} \tag{35}$$

where $\Delta t^{n+1/2} = \frac{\Delta t^n + \Delta t^{n+1}}{2}$. The deformed geometry is updated by adding the displacement increments to the initial geometry

$$\underline{x}_{n+1} = \underline{X} + \underline{u}_{n+1} \tag{36}$$

1. Committed state at time t_n

$$\left\{\boldsymbol{E}_n^p, \boldsymbol{\Sigma}_n, f_n, \bar{\boldsymbol{\sigma}}_n, \Phi_n\right\}$$

2. Given a strain increment $\Delta\boldsymbol{E}$ at time t_{n+1},

$$\Delta\boldsymbol{\Sigma}^{trial} = \mathbb{C}^{hom} : \Delta\boldsymbol{E},$$
$$\boldsymbol{\Sigma}^{trial} = \boldsymbol{\Sigma}_n + \Delta\boldsymbol{\Sigma}^{trial}$$

determine the corresponding stress $\boldsymbol{\Sigma}_{n+1}, \boldsymbol{E}_{n+1}^p$; → goto step 3

3. Check for plastic-damage loading using equation (20)

$$\Phi_{n+1} = \Phi(\boldsymbol{\Sigma}^{trial}, f_n, \bar{\boldsymbol{\sigma}}_n)$$

If $\Phi_{n+1} \leq 0$, this is an elastic step;
set $\boldsymbol{\Sigma}_{n+1} = \boldsymbol{\Sigma}^{trial}, \Delta\boldsymbol{E}^p = \boldsymbol{0}, \Delta f = 0, \bar{\boldsymbol{\sigma}}_{n+1} = \bar{\boldsymbol{\sigma}}_n \rightarrow$ exit
Else, this is a plastic step;→ goto step 4

4. Return mapping at time step t_{n+1}
set $\boldsymbol{\Sigma}_{n+1} = \boldsymbol{\Sigma}^{trial}$
For $iter = 1 : niter$
$\boldsymbol{g} = \partial\Phi/\partial\boldsymbol{\Sigma}_{n+1}$
$$\Delta\lambda = \frac{\bar{\sigma}^2}{\gamma\, \Sigma_{eq}^{trial}} \left(\frac{3\mathcal{R}}{6\mathcal{R} + 4f\sinh\mathcal{R}}\right) \boldsymbol{g} : \mathbb{C}^{hom} : \Delta\boldsymbol{E}$$
$\Delta\boldsymbol{E}^p = \Delta\lambda\, \mathbb{C}^{hom} : \boldsymbol{g}$
update $\mathbb{C}^{cons}$ using equation (32)
$\Delta\boldsymbol{\Sigma} = \mathbb{C}^{cons} : \Delta\boldsymbol{E}$
$\boldsymbol{\Sigma}_{n+1} = \boldsymbol{\Sigma}_n + \Delta\boldsymbol{\Sigma}$
update f_{n+1} and $\bar{\boldsymbol{\sigma}}_{n+1}$
If $\Phi(\boldsymbol{\Sigma}_{n+1}, f_{n+1}, \bar{\boldsymbol{\sigma}}_{n+1}) \leq 10^{-6}$; → break
End

Figure 5. Return mapping algorithm.

During the updating procedure, a new time step size is calculated by taking the minimum value over all elements. The time step size is limited by the Courant-criterion by

$$\Delta t \leq \alpha\ \Delta t_{\text{crit}} = \alpha \frac{2}{\omega_{\max}} \tag{37}$$

where $\omega_{\max}$ is the largest eigen-frequency. The COURANT-criterion is based on linear problems, so in order to consider nonlinearities, the factor $\alpha \leq 1$ is introduced. For moderately nonlinear applications, usually $\alpha = 0.9$ is sufficient, for applications as, for example, high-speed impact problems, α may have to be 0.9 or smaller value.

The use of the central difference method leads to a system of uncoupled linear equations and only vector operations are performed on global level if diagonal mass matrices are used. This leads to very little Central Processing Unit (CPU)-time requirements per time step, compared to implicit methods.

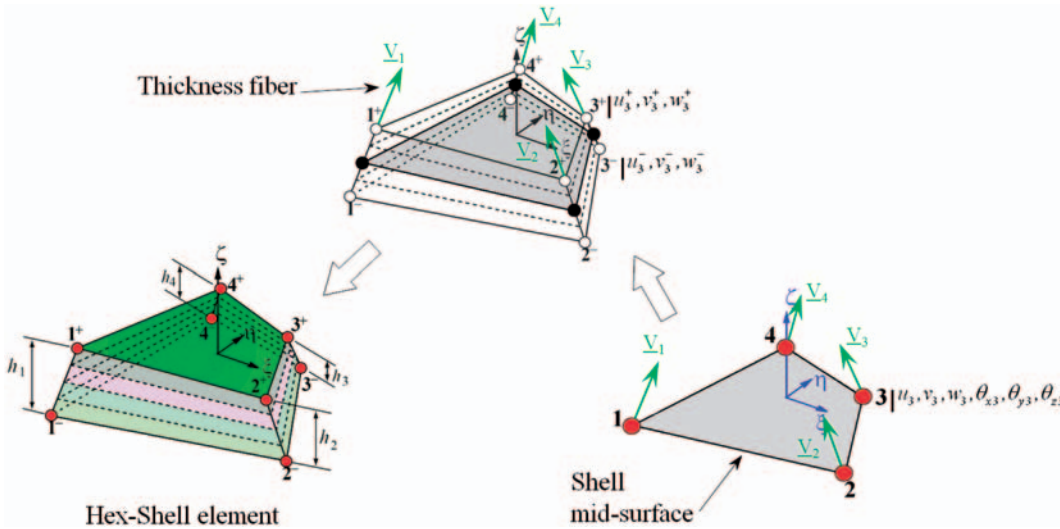

Figure 6. Eight-node hex-shell element.

Kinematics of the 8-node hex-shell model

In this section, the formulation of the 8-node hex-shell element is briefly recalled. With respect to nodal designation (Figure 6), the coordinate vector $\underline{x}$ and displacement vector $\underline{u}$ of the element are (Naceur et al., 2013):

$$\underline{x} = \underline{\tilde{x}}(\xi,\eta) + \frac{\zeta}{2}\underline{V}(\xi,\eta) = \sum_{i=1}^{4} N_i(\xi,\eta)\left(\frac{1-\zeta}{2}\underline{x}_i^- + \frac{1+\zeta}{2}\underline{x}_i^+\right) \tag{38}$$

$$\underline{u} = \sum_{i=1}^{4} N_i(\xi,\eta)\left(\frac{1-\zeta}{2}\underline{u}_i^- + \frac{1+\zeta}{2}\underline{u}_i^+\right) \tag{39}$$

where $\underline{\tilde{x}}$ is the position vector at the mid-surface, $\hat{h}$ and $\underline{\hat{n}}$ are the average thickness and the normal of the sheet, respectively, $N_i(\xi,\eta)$ are the two-dimensional 4-node Lagrangian interpolation functions, $\underline{x}_i^-$, $\underline{u}_i^-$ and $\underline{x}_i^+$, $\underline{u}_i^+$ are respectively, the coordinate and displacement vectors of the ith node on the bottom and top shell surfaces (Figure 6).

In this work, linear, isoparametric hex-shell elements are used with bilinear interpolation in membrane and linear interpolation in thickness direction.

When dealing with structures under large displacement, it is commonly useful to use the Green–Lagrange measure to quantify strains

$$\mathbf{E} = \frac{1}{2}\left(\mathbf{F}^T\mathbf{F} - \mathbf{I}\right) \tag{40}$$

with $\mathbf{F} = \mathbf{I} + \mathbf{L}$ the deformation gradient. The displacement gradient in the cartesian framework is obtained from its image in the parametric description

$$\mathbf{L} = \mathbf{L}_\zeta \mathbf{F}_\zeta^{-1} \tag{41}$$

$\mathbf{L}_\zeta$ and $\mathbf{F}_\zeta$ are the displacement gradient tensor and the deformation gradient tensor, respectively, they are expressed in the parametric space, and are given by

$$\mathbf{L}_\zeta = [\underline{u}_{,\xi}; \underline{u}_{,\eta}; \underline{u}_{,\zeta}]; \quad \mathbf{F}_\zeta = [\underline{a}_{1\zeta}; \underline{a}_{2\zeta}; \underline{a}_{3\zeta}] \tag{42}$$

with the contravariant basis vectors $\underline{a}_{1\zeta} = \underline{\tilde{x}}_{,\xi} + \frac{1}{2}\zeta \underline{V}_{,\xi}$, $\underline{a}_{2\zeta} = \underline{\tilde{x}}_{,\eta} + \frac{1}{2}\zeta \underline{V}_{,\eta}$ and $\underline{a}_{3\zeta} = \frac{1}{2}\zeta \underline{V}$.

Cartesian components of the Green–Lagrange strain tensor $\mathbf{E}$ can be related to the curvilinear strain tensor $\mathbf{E}_t$ using the orthonormal transformation operator $\mathbf{Q} = [\underline{t}_{1\zeta}; \underline{t}_{2\zeta}; \underline{n}_\zeta]$, it can also be connected to the covariant basis $\mathbf{E}_\xi$, using

$$\mathbf{E}_t = \mathbf{Q}^T \mathbf{E} \mathbf{Q}; \quad \mathbf{E} = \mathbf{F}_\zeta^{-T} \mathbf{E}_\xi \mathbf{F}_\zeta^{-1} \tag{43}$$

Using equation (43), one can obtain a direct relationship between curvilinear and the covariant strains

$$\mathbf{E}_t = \mathbf{C}_\zeta^T \mathbf{E}_\xi \mathbf{C}_\zeta \tag{44}$$

with $\mathbf{C}_\zeta = \mathbf{F}_\zeta^{-1}\mathbf{Q}$, and the covariant components of the Green–Lagrange strain tensor are

$$\begin{aligned}
E_{\xi\xi} &= \underline{a}_{1\zeta} \cdot \underline{u}_{,\xi} + \frac{1}{2}\underline{u}_{,\xi} \cdot \underline{u}_{,\xi}; \quad 2E_{\xi\eta} = \underline{a}_{1\zeta} \cdot \underline{u}_{,\eta} + \underline{a}_{2\zeta} \cdot \underline{u}_{,\xi} + \underline{u}_{,\xi} \cdot \underline{u}_{,\eta} \\
E_{\eta\eta} &= \underline{a}_{2\zeta} \cdot \underline{u}_{,\eta} + \frac{1}{2}\underline{u}_{,\eta} \cdot \underline{u}_{,\eta}; \quad 2E_{\xi\zeta} = \underline{a}_{1\zeta} \cdot \underline{u}_{,\zeta} + \underline{a}_{3\zeta} \cdot \underline{u}_{,\xi} + \underline{u}_{,\xi} \cdot \underline{u}_{,\zeta} \\
E_{\zeta\zeta} &= \underline{a}_{3\zeta} \cdot \underline{u}_{,\zeta} + \frac{1}{2}\underline{u}_{,\zeta} \cdot \underline{u}_{,\zeta}; \quad 2E_{\eta\zeta} = \underline{a}_{2\zeta} \cdot \underline{u}_{,\zeta} + \underline{a}_{3\zeta} \cdot \underline{u}_{,\eta} + \underline{u}_{,\eta} \cdot \underline{u}_{,\zeta}
\end{aligned} \tag{45}$$

Principle of virtual work: Internal force vector

In order to deal with the several lockings separately, we need to separate the expression of virtual internal work by uncoupling the membrane/bending, transverse/thickness and shearing (Naceur et al., 2013)

$$W_{\text{int}} = \sum_{e=1}^{\text{nelt}} W_{\text{int}}^e; \quad W_{\text{int}}^e = W_{\text{int}}^{\text{mb}} + W_{\text{int}}^{\text{tr}} + W_{\text{int}}^{\text{sh}} \tag{46}$$

$$W_{\text{int}}^{\text{mb}} = \int_{V^0} \delta\mathbf{E}_{\text{mb}} : \mathbf{S}_{\text{mb}} \mathrm{d}V = \delta\underline{u}^T \underline{f}_{\text{int}}^{\text{mb}}; \quad \underline{f}_{\text{int}}^{\text{mb}} = \int_{V^0} \mathbf{B}_{\text{mb}}^T \mathbf{S}_{\text{mb}} \mathrm{d}V \tag{47}$$

$$W_{\text{int}}^{\text{tr}} = \int_{V^0} \delta\mathbf{E}_{\text{tr}} : \mathbf{S}_{\text{tr}} \mathrm{d}V = \delta\underline{u}^T \underline{f}_{\text{int}}^{\text{tr}}; \quad \underline{f}_{\text{int}}^{\text{tr}} = \int_{V^0} \mathbf{B}_{\text{tr}}^T \mathbf{S}_{\text{tr}} \mathrm{d}V \tag{48}$$

$$W_{\text{int}}^{\text{sh}} = \int_{V^0} \delta\mathbf{E}_{\text{sh}} : \mathbf{S}_{\text{sh}} \mathrm{d}V = \delta\underline{u}^T \underline{f}_{\text{int}}^{\text{sh}}; \quad \underline{f}_{\text{int}}^{\text{sh}} = \int_{V^0} \mathbf{B}_{\text{sh}}^T \mathbf{S}_{\text{sh}} \mathrm{d}V \tag{49}$$

with $\mathbf{E}$ the Green–Lagrange strain tensor split into three tensors, namely the membrane/bending tensor $\mathbf{E}_{mb}$, defined by the components E_{11}, E_{22}, E_{12}, the transverse tensor $\mathbf{E}_{tr}$, defined mainly by three components E_{11}, E_{22}, E_{33} and the shearing tensor $\mathbf{E}_{sh}$ defined by the shearing strains E_{13}, E_{23}. The second Piola Kirchhoff Stress tensor $\mathbf{S}$ is also decomposed into three parts, $\mathbf{S}_{mb}$, $\mathbf{S}_{tr}$ and $\mathbf{S}_{sh}$. The internal force vector at the element level is then given by

$$\underline{f}_{int}^{u} = \underline{f}_{int}^{mb} + \underline{f}_{int}^{tr} + \underline{f}_{int}^{sh} \tag{50}$$

A hex-shell element formulated using equations equations (47) to (49) with standard integration based on a 2×2 Gauss schema in the in-plane of the shell element, will fail because of numerous locking phenomena.

Remedies for shear locking. An effective method of resolving shear locking is the ANS method in which the natural transverse shear strains are sampled (Figure 7) and then interpolated at some discrete element points with a specific order.

The transverse shear strains $E_{\xi\zeta}$ and $E_{\eta\zeta}$ are calculated according to the average surface plan ($\zeta = 0$), assuming that they vary linearly, and are functions of E_{ξ} and E_{η} at the mid-side points

$$E_{\xi\zeta}^{ANS} = \frac{1-\eta}{2} E_{\xi}^{A1} + \frac{1+\eta}{2} E_{\xi}^{A2}; \quad E_{\eta\zeta}^{ANS} = \frac{1-\xi}{2} E_{\eta}^{B1} + \frac{1+\xi}{2} E_{\eta}^{B2} \tag{51}$$

Remedies for trapezoidal locking. Similar to shear locking, trapezoidal locking occurs when lower order elements such as 8-node hexahedral elements are used to model curved shells so that their cross-sections assume the trapezoidal shape. These excessive numbers of sampled thickness strains can be reduced by using a bilinear interpolation of the transverse normal strains sampled at the four corners of the element mid-surface (Figure 8), namely

$$E_{\zeta\zeta}^{ANS} = \sum_{i=1}^{4} N_i(\xi, \eta) E_{\zeta\zeta}(\xi_i, \eta_i) \tag{52}$$

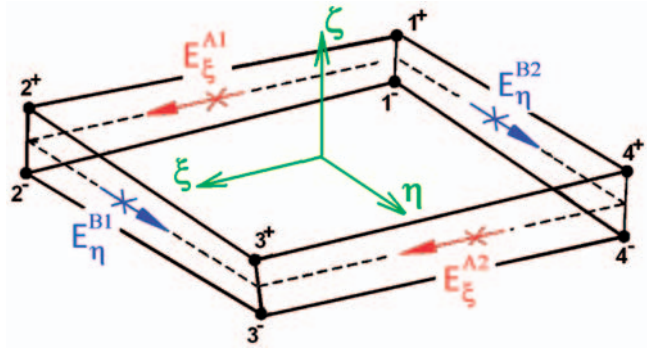

Figure 7. Shear locking treatment using ANS method.

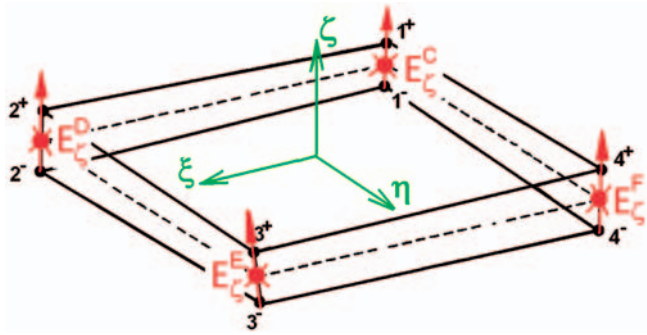

Figure 8. Trapezoidal locking treatment using ANS method.

Remedies for volumetric locking. Material locking is controlled by a material parameter, the Poisson ratio ν.

Poisson's ratio coupling requires the thickness strain to be a linear function of ζ. Because our hex-shell element has only two layers, as consequence the thickness strain does not vary with ζ thus the element fail in reproducing the plane-stress condition.

$$\tilde{E}_{\zeta\zeta}^{\mathrm{EAS}} = E_{\zeta\zeta}^{\mathrm{ANS}} + \alpha\zeta t_{33} \tag{53}$$

where α represents the seventh independent internal parameter which will be eliminated by special condensation technique at the element level, t_{33} is required for transformation to the local element co-ordinates. An additional condition has now to be satisfied locally, leading to the increment of the additional degrees of freedom.

$$\frac{\partial W_{\mathrm{int}}}{\partial \mathbf{u}}\Delta\mathbf{u} + \frac{\partial W_{\mathrm{int}}}{\partial \alpha}\Delta\alpha = -W_{\mathrm{int}}(\mathbf{u},\alpha) \tag{54}$$

On element level, the internal virtual work can now be computed with the compatible and the enhanced strains as in equation (53)

$$W_{\mathrm{int}} = \sum_{i=1}^{nl}\int_{\xi}\int_{\eta}\int_{\zeta_i}^{\zeta_{i+1}} \left(\delta\mathbf{E}_{\mathrm{mb}} : \mathbf{S}_{\mathrm{mb}} + \delta\mathbf{E}_{\mathrm{tr}}^{\mathrm{EAS}} : \mathbf{S}_{\mathrm{tr}} + \delta\mathbf{E}_{\mathrm{sh}}^{\mathrm{ANS}} : \mathbf{S}_{\mathrm{sh}}\right) J\mathrm{d}\xi\mathrm{d}\eta\mathrm{d}\zeta = \delta\underline{u}^{T}\underline{f}_{\mathrm{int}}^{e} \tag{55}$$

nl is the number of layers and ζ_i is the transverse reference coordinate of the i-th layer along the cross-section of the element. The internal force vector $\underline{f}_{\mathrm{int}}^{e}$ can be obtained explicitly using compatible and enhanced strains

$$\underline{f}_{\mathrm{int}}^{e} = \underline{f}_{\mathrm{int}}^{u} - \frac{f_\alpha}{k_{\alpha\alpha}}\underline{k}_{\alpha u} \tag{56}$$

where f_α and $k_{\alpha\alpha}$ can be found in Naceur et al. (2013).

The global internal force vector $\underline{F}$ is then obtained by assembling element internal forces $\underline{f}_{\text{int}}^{e}$

$$\underline{F} = \sum_{e=1}^{\text{nelt}} \underline{f}_{\text{int}}^{e} \tag{57}$$

The use of a full integration in the in-plane of the shell element, through the use of 2×2 Gauss points, allows the obtention of a stiffness matrix that has a correct rank, this reveals that element has no hourglass modes, therefore, stabilisation is not required in the present model. The present 8-node hex-shell element has been already validated and presented in previous research works done by the authors Naceur et al. (2013). It has been shown in previous works, that the present FE model is more efficient than classical brick elements, especially when dealing with moderately thick structures under bending loading.

Application to the failure modelling of human femur

Material and protocol

Twenty-one previously frozen, human cadaveric proximal specimens were obtained (11 right and 10 left) from 19 donors for this study (5 men and 14 women). The femora were initially conserved in a freezer at -21°C. The mean donor age was 87 years (range 63–94). This investigation was approved by the clinical research ethics board at the *University Hospital de la Timone* at Marseille. Anteroposterior standard radiographs of each specimen were obtained and examined by an orthopaedic surgeon for signs of previous fracture and metastatic bone disease.

CT scans for each human cadaveric femora were performed and repeated three times using a LightSpeed VCT scanner from GE Medical Systems. First acquisition was performed prior to preparing the femurs for the mechanical testing with a detector collimation of 41 mm. An additional acquisition was performed on every femur prior to the mechanical tests to extract precisely the boundary conditions. A last scan was performed after the mechanical testing, in order to observe the fracture location in the bone and identify the mechanisms (geometric or architectural) that led to the damage of the femur. The voxel resolution of the femur CT scan was set to: $0.2\,\text{mm} \times 0.2 \times 0.5\,\text{mm}$. While for the specimen extracted from the femoral head, the resolution was 19.8 μm.

Global mechanical testing on proximal femora

The experimental device was designed according to the loading configurations developed by de Bakker et al. (2009) and Manske et al. (2009). The proposed experimental setup is able to simulate a sideways fall on the greater trochanter with a mechanical tension/compression machine shown in Figure 9. The improvements compared to previous experimental setups are mainly in the strict control of boundary conditions. The main objective is to reproduce exactly the experimental conditions in future simulations by FEs.

At the beginning, the shaft of the femur has been immersed in a rigid cylinder using an epoxy resin (type F23 AXSON TECHNOLOGIES), leaving 7.5 cm from the lesser trochanter (Figure 9), in order to strengthen the fixation of the femur into the device. Two threaded rods have been then introduced into the coated shaft to ensure the 15° internal rotation of the femur and put the femoral neck in the coronal plane. A sample holder allowing horizontal translations in Y direction and free

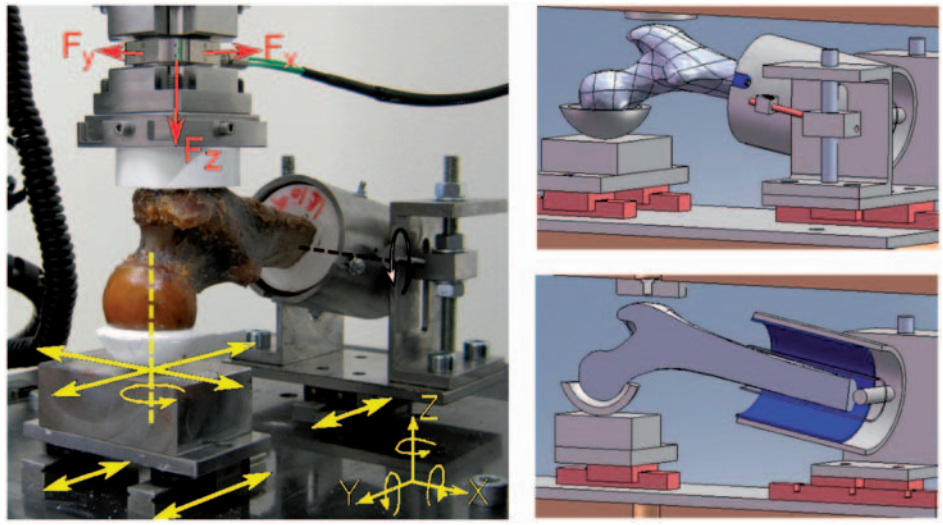

Figure 9. Test set-up of the mechanical testing apparatus. The arrows on the photograph indicate the degrees of freedom at the proximal and distal ends of the femur.

rotations in the coronal plane was designed to maintain the femur shaft at 10° adduction in the apparatus. The head of the femur was supported by a personalised hemispherical epoxy-based shell to distribute the load as evenly as possible over the contact surface (Yoshida et al., 2006) and also to prevent local crushing as it was only constrained from vertical movement. Earlier, mechanical testing have been carried out on the used epoxy resin (type F23 AXSON TECHNOLOGIES) to identify its mechanical properties and their effects on the global behaviour of the femora during the sideways fall testing. The 21 femurs were tested mechanically at room temperature, up to failure under quasi-static conditions using constant vertical displacement of 10 mm/mn through Z direction. The load was applied to the greater trochanter by means of a personalised epoxy cup. The load was measured using a three-component load cell sensor (model KISLTER 9327 A) coupled with a charge amplifier (model KISLTER ICAM 5073). Before the test recording, the specimens have been preloaded to 5 N which was defined as the starting zero reference measurements.

The obtained results are discussed in terms of force and displacement. For each femur, the maximum load in Z direction (F_1) characterising the initial bone's damage and the ultimate load in Z direction (F_2) characterising the bone's fracture are determined. The specific energy (W) is absorbed by the femur until the fracture is also computed.

Local testing of the cancellous bone extracted from the femoral head

As mentioned before, in order to use the micromechanical plastic-based damage model presented in the section 'Formulation of the micromechanics-based ductile damage model of the femur bone', mechanical properties of the trabecular bone have to be identified locally. Namely the Elastic modulus E^m, the initial yield stress σ_y^m and hardening parameters of the local cancellous bone considered here as being the matrix. In order to limit the number of unknown material parameters, in this investigation, the assumption of a linear hardening of the matrix bone is chosen ($\bar{\sigma} = E_T^m \overline{\varepsilon^p}$), leading to an additional variable represented by a constant tangent elastoplastic modulus E_T^m. To this end,

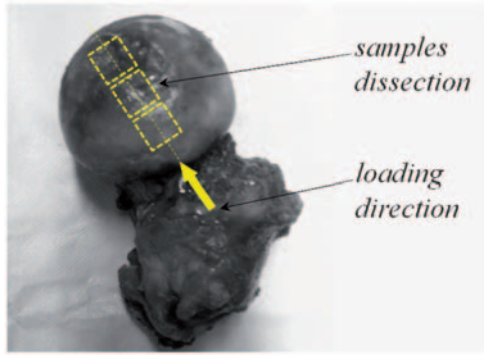

Figure 10. Head femoral dissection for the local study of the trabecular bone mechanical parameters.

three cubic samples of $10 \times 10 \times 10\,mm^3$ were extracted from the same femoral head along the neck axis as shown in Figure 10.

The cancellous bone samples used to determine the model parameters in the present investigation were chosen from the head of the same femur for two reasons: first, because the femoral head contains the maximal porosity in the femur, and the second reason, it was not possible to use the greater trochanter because this region has been submitted to compression using a stiff contactor during the sideways fall experimentation on the femur. At the end of the experiment, the trochanter region was totally compressed and was not suitable for dissection. For the other femurs, we decided to use each femur to identify its own parameters, using its femoral head, this is to avoid inter-individual variability.

The concerned femur is first referenced and the periosteum of the femoral head is removed. The selected area of the head is divided into several sections of 10 mm thickness. A second axial cutting is done in order to obtain three cubic specimens of pure cancellous bone (Figure 10). By means of the X-ray microtomography technique three samples were scanned using a SKYSCAN 1172 micro-scanner with a resolution of 20 μm for the identification of initial porosity. Each of the specimens is instrumented using gauges for strain measurement and provides a load/displacement and stress/strain curves, characteristic of the local mechanical behaviour of the femoral bone. Compression mechanical tests are performed at room temperature (20°C) with a single-column machine type Hounsfield H5KT, controlled by an electric stepper engine as shown in Figure 11.

A cell of 5 kN effort is used. Each specimen is loaded to 50% deformation with a velocity of 10 mm/min. Each test provides a load/displacement curve, characteristic of the mechanical behaviour of the specimen tested.

A summary of the experimentally measured material parameters are given in Table 1. The resulting load–displacement curves obtained from the experimental compression testing on the cubic samples are also given in Figure 12. All compression tests have been done up to 50% of deformation, and as we can notice all three tests gave approximately the same behaviour, with a relatively small elastic zone (up to 2%) and a very small value of the yielding stress (up to 1 MPa), which has been already expected for the cancellous bone.

Numerical identification of local cancellous bone mechanical properties

Based on the above experimental results given in Figure 12, a numerical procedure for the identification of the femur matrix material parameters has been carried out using the developed

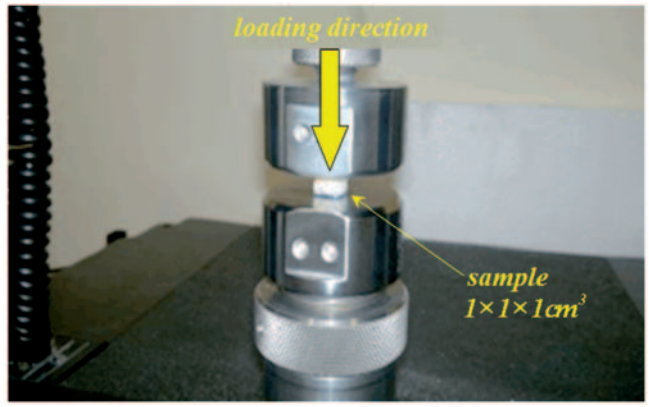

Figure 11. Experimental set-up used for femoral head specimens compression.

Table 1. Summary of the experimentally local measured material parameters.

No. exp.	E (MPa)	ν	f_p (%)
Sample 1	39	0.19	77.95
Sample 2	40	0.19	85.05
Sample 3	50	0.19	87.20
Min–Max	39–50	0.19	77.95–87.20
Mean	**43**	**0.19**	**83.4**

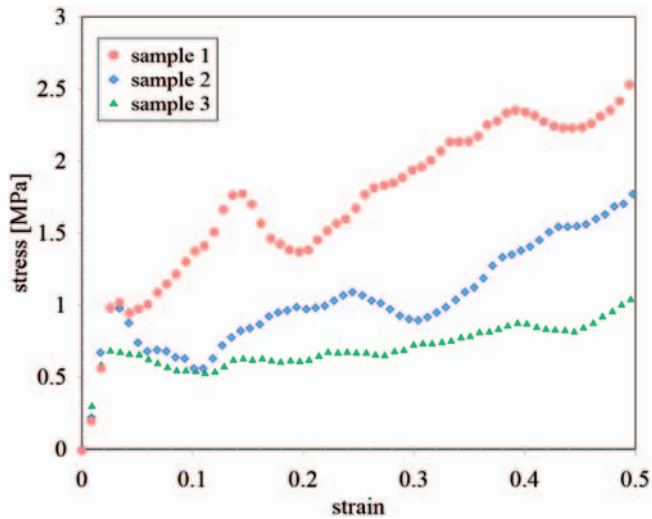

Figure 12. Experimental stress–strain response of the femoral head specimens under compression.

Table 2. Identified material parameters of the cancellous bone in MPa (matrix and homogenised parameters).

No. exp.	E^m	σ_y^m	E_T^m	E^{hom}	E^{exp}	σ_y^{hom}
Sample 1	304	6.13	8.25	40.21	39	1.04
Sample 2	425	5.52	6.34	39.57	40	0.99
Sample 3	517	5.34	3.22	48.83	50	0.68
Mean	**415**	**5.67**	**5.93**	**42.87**	**43**	**0.90**

homogenised hex-shell element based on MCK criterion (Monchiet et al., 2011) and implemented within user routine UMAT in LS − DYNA© software. In the present inverse identification the cubic samples were meshed using $10 \times 10 \times 10$ hex-shell elements, and compression was performed using a controlled velocity of 10 mm/min. Each specimen was loaded up to 90% deformation.

For the inverse identification, we used a Sequential Quadratic Programming algorithm (Zhang and Zhang, 2003) in order to perform the fitting of computed results with the experimental measurements by finding the optimal set of constitutive parameters, namely the Young's modulus E^m, the initial yield stress σ_y^m and the tangent elastoplastic modulus E_T^m of the matrix bone. The void volume fraction was measured by microtomography for each sample as reported in Table 1. The aspect ratio is taken $w = 1$, which corresponds to the assumption of spherical voids of the local cancellous bone inside the femoral head. In this investigation, Poisson ratio was not studied and was fixed equal to the experimental measured value of 0.19 as reported in Table 1.

Table 2 summarises the obtained results using the inverse identification procedure. As we can observe, the identified Young's modulus E^m of the cancellous matrix bone shows slight variations from 304 MPa to 517 MPa with an average value of 415 MPa, this is a direct consequence of the variations observed on the measurement data themselves.

The same conclusions could be drawn, from the observation of the identified initial yield stress σ_y^m and the tangent elastoplastic modulus E_T^m of the matrix bone in the femoral head, which varies from 5.34 MPa to 6.13 MPa and from 3.22 MPa to 8.25 MPa, respectively. These results are also presented in the form of stress–strain curves in Figure 14. One can observe that even with the assumption of a linear hardening of the matrix bone $\bar{\sigma} = E_T^m \overline{\varepsilon^p}$, the obtained model response after yielding presents a strong nonlinear character. This is due to the cancellous bone densification effects, generally observed in compression testing of cellular materials. Mean values of the Young's modulus $E^m = 415$ MPa, the yield stress $\sigma_y^m = 5.67$ MPa and the tangent elastoplastic modulus $E_T^m = 5.93$ MPa, allow obtaining the average 'bold-black' stress–strain curve shown in Figure 14. These average values are used as bone material data in the present model to carry out a global compression testing on the femora.

Numerical validation using the global testing on proximal femur

The final stage is a numerical validation of the implemented MCK model, through the use of a global sideways fall on the greater trochanter as exposed in the section 'Global mechanical testing on proximal femora'. The first step in this phase was the reconstruction of the 3D geometry of the femur starting from the digitalised STL inner and outer surfaces of the femur. As shown in Figure 15, the digitalised STL mesh was split into two different parts (inner and outer surfaces).

The outer surface is constituted by cortical bone of initial porosity $f_p = 10\%$ and the inner one by trabecular bone of initial porosity $f_p = 77\%$, obtained using a SKYSCAN 1172 microscanner. Then each STL surface was partitioned along the transverse direction into small parts (Figure 15) using

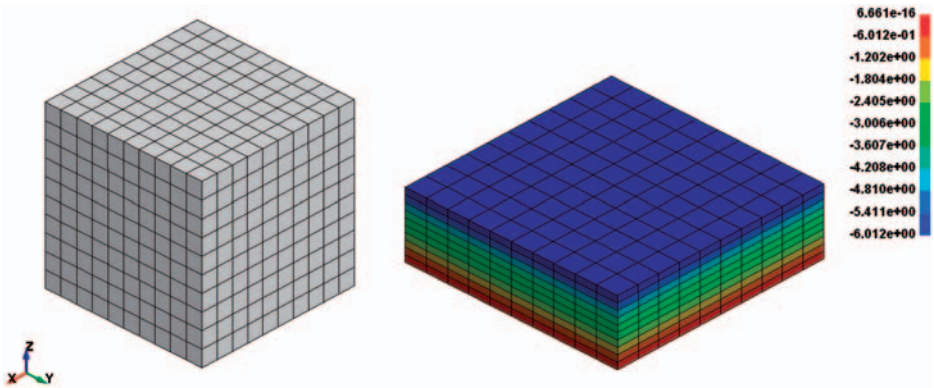

Figure 13. FE mesh using 10 × 10 × 10 homogenised hex-shell elements for the REV modelling.

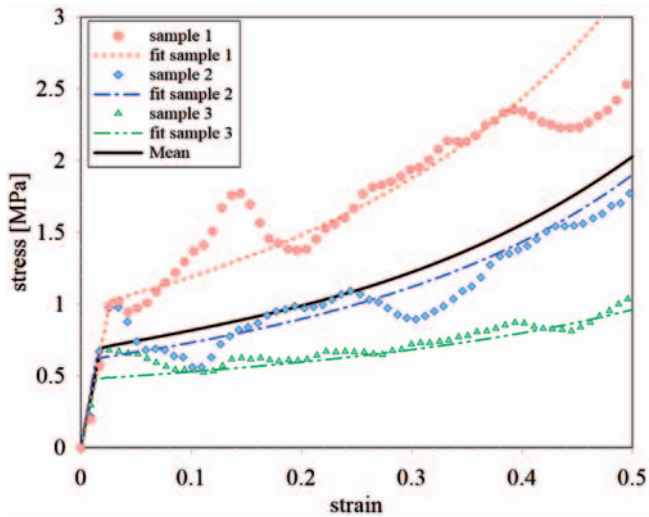

Figure 14. Numerical vs. experimental results obtained for the femoral head specimens under compression test.

HYPERMESH© software (Altair Engineering, 2013). The small local surfaces are developed based on their edges which have been regenerated thanks to HYPERMESH© CAD facilities. Once the total inner and outer surfaces of the femur are built up, a first mapped shell mesh is generated using only quadrilateral shell elements. Then a 3D mesh of the femur volume is generated with hexahedra, thanks to the 3D meshing facilities available in HYPERMESH© software (see Figure 15).

The total mesh of the femur includes 7400 hex-shell elements. The FE simulation was carried out using the Explicit Dynamic algorithm within LS – DYNA© code, with a total running CPU time of 8 min 46 s using a Dell Precision PWS690 workstation with two 64-bit Quad-Core Intel Xeon processors of 2.66 GHz and 8 GB of RAM. Figure 16 shows the load–displacement response of the modelled femur compared to the corridor obtained experimentally using the set of 21 tested femurs. We can observe globally, that a good agreement is obtained for the estimation of the ultimate load supported by the femur before collapse.

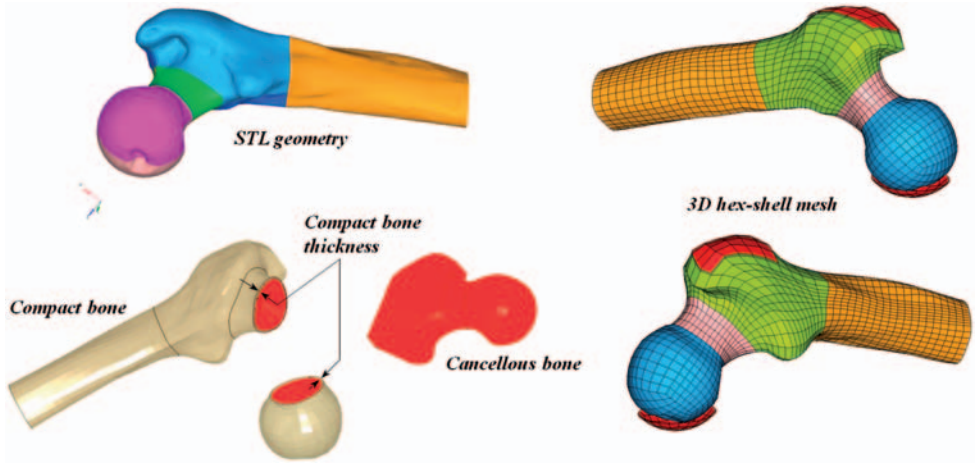

Figure 15. Proximal femur CAD geometry and FE mesh using 7400 hex-shell elements.

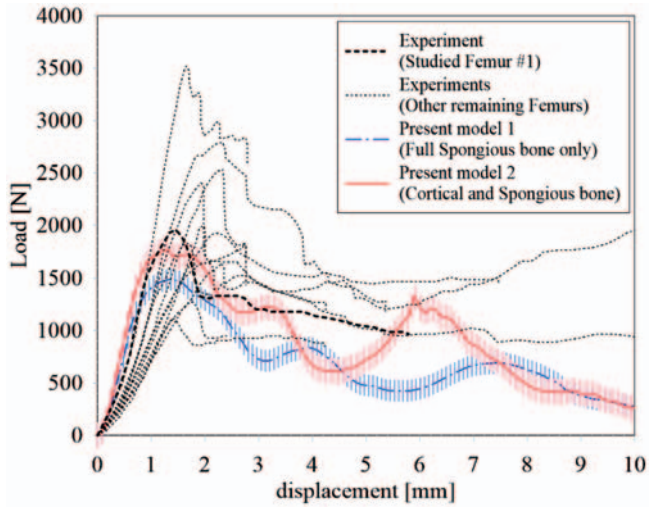

Figure 16. Load–displacement femora response: Expreimental vs. numerical comparison.

Moreover, from Figure 17, we can observe that the damage evolution was started locally at the superior cortex of femoral neck (see Figure 17(d)). As the load augmented, the damage starts invading the inferior tensile side of femoral neck. Then due to maximum tensile and compressive strains, the damage propagated rapidly to the lower surface following a diagonal path, resulting almost a complete separation of the proximal femur at the end (Figure 17(h)).

Predicted proximal femur rupture shape consistent with different cracks propagation stages in relation with the load–displacement response is shown in Figure 18. The damage started at the upper compression side at a stroke of 3 mm (Figure 17(d)), then it spreads gradually until a stroke of 5 mm (Figure 17(f)) where the upper crack starts to bifurcate towards the lower tensile side of the femoral

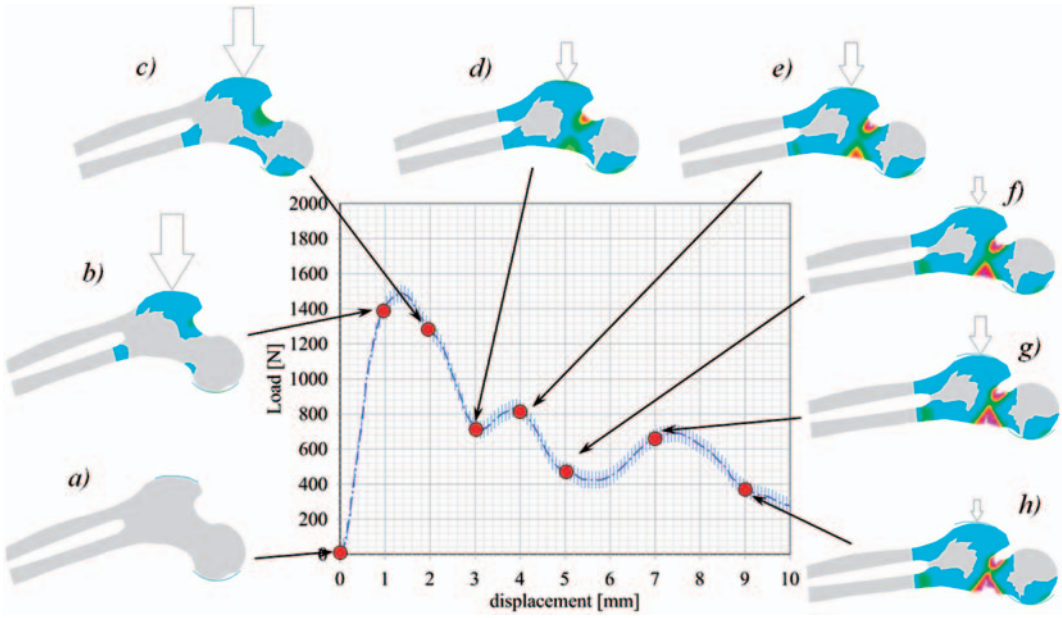

Figure 17. Damage evolution in the cancellous femoral bone during compression. (a) Femur at the initial position before loading; (b) Femur loaded until the initial yield stress is reached; (c) First buckling and damage initiation starting at the superior cortex of femoral neck; (d) Damage propagation at the superior cortex of femoral neck; (e) Second buckling and damage initiation starting at the inferior cortex of femoral neck; (f) Crack initiation at the superior cortex of femoral neck; (g) Crack initiated close to the greater trochanter at the lower tensile side and (h) Complete separation of the proximal femur at the end (basicervical fracture).

neck. At a stroke of 7 mm (Figure 17(g)) the crack is initiated almost close to the greater trochanter at the lower tensile side, and grows quickly towards the upper compression side resulting in almost a complete separation of the proximal femur in the form of basicervical fracture at a stroke of 9 mm (Figure 17(h)).

Basicervical fractures are a specific kind of hip fracture taking place at the base of the neck of the proximal femur. The fracture path goes through the femoral neck nearby to the trochanter. Basicervical fracture (Figure 18) is a debatable sort of hip fracture, which can be viewed as either high intertrochanteric fractures (Guss, 1997) or low neck fractures (Konishiike et al., 1999). It lacks a precise definition in the most commonly used classifications.

Discussion and limitations

While the present investigation emphasised the capabilities of a newly proposed micromechanical model for the prediction of the human proximal femora ultimate load and its fracture pattern; however the underlying micromechanical model still has some limitations. Even though, it employed only five material parameters (elastic modulus, yield stress and tangent modulus of the matrix, the aspect ratio and the porosity) to describe accurately a very complex behaviour of a human bone, some of these parameters are difficult to measure directly because they have been introduced using somehow strong assumptions. For instance, it is assumed in the present investigation, that the bone matrix properties are the same for the cancellous and the cortical bone and therefore the differences

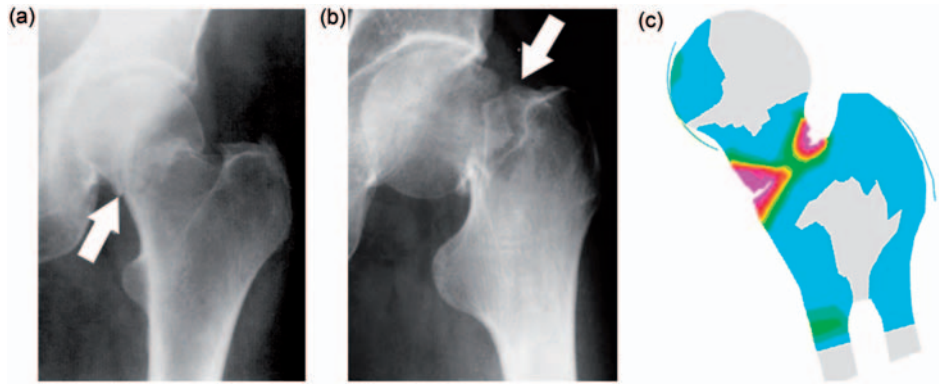

Figure 18. Qualitative comparison between predicted fracture zone and examples of typical basicervical fracture from Guss (1997) and Konishiike et al., 1999. (a) Example of a radiograph of a 78-year-old woman with a femoral neck fracture from Guss (1997). (b) Radiograph of a 56-year-old man with a type-A displaced fracture from Konishiike et al. (1999). (c) Predicted fracture profile using the MCK damage model.

in the stiffness come only from the porosity factor i.e. the volume void fraction as well as from the voids architecture and orientations. It is well known that trabecular bone has more connected network of pores than cortical bone. Specifically, cortical bone porosity consists primarily of cylindrical canals serving the vascular system (i.e. longitudinal Haversian canals and transverse Volkmann canals). Though for the sake of simplicity, it has been assumed only one family of ellipsoidal voids to represent both cortical and trabecular bones, where the average size was determined thanks to the CT-scan measure of the porosity and the Mean-Intercept-Length giving the 3D orientations of voids. Indeed, it was possible to include several families of voids or inclusions of different shapes such as: one family of ellipsoidal voids for the trabecular bone and a second family of cylindrical cavities for the cortical bone. This will certainly improve the global response of the bone but at the same time will increase the computational time necessary for the homogenisation procedure. Another alternative would be the use of only one family of ellipsoidal voids but introducing two different aspect ratios of the ellipsoid. An average value of the aspect ratio close to 1 will be given to the cancellous bone, while a higher value the aspect ratio 100 will be given to the cortical bone, stretching the ellipsoid to tend a cylindrical shape. Aside from their importance upon the global response of the proposed model, micromechanical plastic parameters represented by the yield stress and the tangent modulus of the matrix bone, have to be determined more precisely using direct measurements such as nano-indentation which will bring more local details of the bone and hence enrich the hardening micromechanical model. While in the present investigation authors use the inverse method to identify the former parameters, the obtained results show that the proposed model can describe accurately the global behaviour of human proximal femora.

A last point concerning the introduction of solid-shell elements, it is well known that classical solid FEs are not appropriate to model thin structures. Additionally, the more thinner the layer is, the higher the number of solid elements will be needed. Therefore, one solution would be the use of at least five tetrahedral elements in the thickness of the cortical layer, if one needs to achieve good results. Then, a second problem arises, corresponding to the element size transition between the cancellous and the cortical regions. The use of only classical solid FEs for the modelling of long bones (including cortical and cancellous) may overestimate the overall stiffness, unless a special care

is given and a fine mesh is used in the relatively thin cortical region. An alternative would be the use of prismatic solid-shell FEs, which can be generated automatically and are of a higher accuracy than classical tetrahedral FEs. Therefore, the cancellous region will be modelled with classical tetrahedral solid elements and the external thin cortical bone will be modelled using only one or two prismatic solid-shell to achieve to a good accuracy at a reasonable cost.

Conclusion

The goal of this investigation was to develop, implement and validate a useful hex-shell FE based on the MCK micromechanical damage model in order to simulate the complete response and the pattern of the fractured area of proximal femur.

The framework of homogenisation was used to derive a yield criterion using an approximate limit-analysis based on the MCK criterion for porous biological materials. The elastic properties of these materials were determined by a coupling from the Mori–Tanaka scheme and experimental measurements of 3D anisotropy using microtomography techniques. The model takes into account the anisotropic behaviour (resulting from the architectural nature of the cancellous bone) coupled to ductile damage to describe the progressive crack initiation and propagation within proximal femoral. The model has been implemented into LS-DYNA code via the user material subroutine UMAT.

To illustrate the potential of the current approach, a right adult human femur was simulated until complete fracture under sideways loading. Predicted load–displacement response shows a same tendency as those observed experimentally. Our results predicted progressive fracture profiles depending on the vertical trochanter stroke. The predicted fracture path follows a diagonal line from the inner surface of the neck (basal) to the outer surface towards the greater trochanter. A comparison between predicted fracture path and radiographs of basicervical fractures from the literature shows a quite good agreement, even if loading conditions (unknown for the radiograph) may be different.

The main ambition of the present investigation was to show the potential of the proposed MCK micromechanical model taking into account the anisotropic behaviour and ductile damage to predict the human proximal femora response and its ultimate load as well as the fracture pattern. The progressive changes in bone microarchitecture and material properties attributed to elderly, may be included into the micromechanical model for a more accurate predictions to evaluate the hip fracture risk of elderly population.

Further improvements will be performed into the present model to be able to simulate the bone behaviour by taking into account the strain rate effects to assess hip fracture accruing due to falls or in sports accidents.

Acknowledgements

The authors are thankful to Rémi Delille and Denis Lesueur, laboratory engineers at LAMIH, for their kind help in the dissection of the head femoral and the DMA testing of local characterisation.

Conflict of interest

The authors declare that they do not have any financial or personal relationships with other people or organisations that could have inappropriately influenced this study.

Funding

This study was supported by CISIT (International Campus on Safety and Intermodality in Transportation) at Valenciennes in France.

References

Altair Engineering (2013) *HYPERMESH© User's Guide Version 11*. Edition: Altair Engineering Inc, 2450 pages, 1820 E. Big Beaver, Troy MI 48083, USA.

Aoubiza B, Crolet J and Meunier A (1996) On the mechanical characterization of compact bone structure using homogenization theory. *Journal of Biomechanics* 29(6): 1539–1547.

Arnoux P, Bonnoit J, Chabrand P, et al. (2002) Numerical damage models using a structural approach: Application to bones and ligaments. *European Physical Journal Applied Physics* 17: 65–73.

Benzley SE, Perry E, Merkley K, et al. (1995) A comparison of all-hexahedral and all-tetrahedral finite element meshes for elastic and elasto-plastic analysis. In: Tautges TJ (ed.) *Proceedings of the 4th International Meshing Roundtable*. Albuquerque, New Mexico, USA, 16–17 October 1995, Sandia National Laboratories, pp. 179–191.

Bessho M, Ohnishi I, Matsuyama J, et al. (2007) Prediction of strength and strain of the proximal femur by a CT-based finite element method. *Journal of Biomechanics* 40: 1745–1753.

Chaboche JL (2013) Multi-scale analysis of polycrystalline metals and composites [chapter 3]. In: Denier JP and Finn MD (eds) *Mechanics Down Under*. The Netherlands: Springer, pp. 35–56.

Christen D, Webster DJ and Müller R (2010) Multiscale modelling and nonlinear finite element analysis as clinical tools for the assessment of fracture risk. *Philosophical Transactions Series A: Mathematical, Physical, and Engineering Sciences* 368(1920): 2653–2668.

Cifuentes AO and Kalbag A (1992) A performance study of tetrahedral and hexahedral elements in 3-D finite element structural analysis. *Finite Elements in Analysis and Design* 12: 313–318.

Cody DD, Gross GJ, Hou FJ, et al. (1999) Femoral strength is better predicted by finite element models than QCT and DXA. *Journal of Biomechanics* 32: 1013–1020.

Courtney AC, Wachtel EF, Myers ER, et al. (1995) Age-related reductions in the strength of the femur tested in a fall-loading configuration. *Journal of Bone and Joint Surgery* 77-A387395.

Courtney AC, Wachtel EF, Myers ER, et al. (1994) Effects of loading rate on strength of the proximal femur. *Calcified Tissue International* 55: 53–58.

Cristofolini L, Taddei F, Baleani M, et al. (2008) Multiscale investigation of the functional properties of the human femur. *Philosophical Transactions Series A: Mathematical, Physical, and Engineering Sciences* 366(1879): 3319–3341.

Cristofolini L, Juszczyk M, Taddei F, et al. (2009) Strain distribution in the proximal human femoral metaphysis. *Proceedings of the Institution of Mechanical Engineers Part H: Journal of Engineering in Medicine* 223(3): 273–288.

Cummings SR and Melton LJ (2002) Epidemiology and outcomes of osteoporotic fractures. *Journal of Lancet* 359: 1761–1767.

De Bakker PM, Manske SL, Ebacher V, et al. (2009) During sideways falls proximal femur fractures initiate in the superolateral cortex: Evidence from high-speed video of simulated fractures. *Journal of Biomechanics* 42(12): 1917–1925.

Ford CM, Keaveny TM and Hayes WC (1996) The effect of impact direction on the structural capacity of the proximal femur during falls. *Journal of Bone and Mineral Research* 11: 377–383.

Gurson AL (1977) Continuum theory of ductile rupture by void nucleation and growth: Part I. Yield criterion and flow rules for porous ductile media. *Journal of Engineering Materials and Technology* 99: 2–15.

Guss DA (1997) Hip fracture presenting as isolated knee pain. *Annals of Emergency Medicine* 29(3): 418–420.

Harnau M and Schweizerhof K (2002) A systematic development of solid-shell element formulation for linear and non-linear analysis employing only displacement degrees of freedom. *International Journal for Numerical Methods in Engineering* 42: 49–69.

Keyak JH (2001) Improved prediction of proximal femoral fracture load using nonlinear finite element models. *Medical Engineering and Physics* 23: 165–173.

Koivumäki JEM, Thevenot J, Pulkkinen P, et al. (2012) Ct-based finite element models can be used to estimate experimentally measured failure loads in the proximal femur. *Bone* 50: 824–829.

Konishiike T, Makihata E, Tago H, et al. (1999) Acute fracture of the neck of the femur. An assessment of perfusion of the head by dynamic MRI. *Journal of Bone and Joint Surgery* 81-b(4): 596–599.
Lenaerts L and van Lenthe GH (2009) Multi-level patient-specific modelling of the proximal femur. A promising tool to quantify the effect of osteoporosis treatment. *Philosophical Transactions Series A: Mathematical, Physical, and Engineering Sciences* 367(1895): 2079–2093.
Li X, Du Y and Duan Q (2013) Micromechanically informed constitutive model and anisotropic damage characterization of Cosserat continuum for granular materials. *International Journal of Damage Mechanics* 22: 643–682.
Liu L (2010) Solutions to the periodic Eshelby inclusion problem in two dimensions. *Mathematics and Mechanics of Solids* 15(5): 557–590.
Livermore Software Technology Corporation (2007) LSDYNA© *keyword user's manual Version 971*. Edition: Livermore Software Technology Corporation (LSTC), 2206 pages, 7374 Las Positas Road Livermore, CA, USA.
Lotz JC and Hayes WC (1990) The use of quantitative computed tomography to estimate risk of fracture of the hip from falls. *Journal of Bone and Joint Surgery* 72-A: 689–700.
Manske SL, Liu-Ambrose T, Cooper DML, et al. (2009) Cortical and trabecular bone in the femoral neck both contribute to proximal femur failure load prediction. *Osteoporosis International* 20(3): 445–453.
Marshall D, Johnell O and Wedel H (1996) Meta-analysis of how well measures of bone mineral density predict occurrence of osteoporotic fractures. *British Medical Journal* 312: 1254–1259.
Monchiet V, Charkaluk E and Kondo D (2011) A micromechanics-based modification of the Gurson criterion by using Eshelby-like velocity fields. *European Journal of Mechanics A/Solids* 30: 940–949.
Mori T and Tanaka K (1973) Averages stress in matrix and average elastic energy of materials with misfitting inclusions. *Acta Metallia* 21: 571–574.
Naceur H, Shiri S, Coutellier D, et al. (2013) On the modeling and design of composite multilayered structures using solid-shell finite element model. *Finite Elements in Analysis and Design* 701–7114.
Nedoushan RJ, Farzin M and Mashayekhi M (2013) A micro-structural model for prediction of void initiation in superplastic forming. *International Journal of Damage Mechanics* 22: 1206–1221.
Niazi MS, Wisselink HH, Meinders T, et al. (2012) Failure predictions for DP steel cross-die test using anisotropic damage. *International Journal of Damage Mechanics* 21: 713–754.
Oral A, Anlas G and Lambros J (2012) Determination of GursonTvergaardNeedleman model parameters for failure of a polymeric material. *International Journal of Damage Mechanics* 21: 3–25.
Pinilla TP, Broadman KC, Bouxsein ML, et al. (1996) Impact direction from a fall influences the failure load of the proximal femur as much as agerelated bone loss. *Calcified Tissue International* 58: 231–235.
Rahmoun J, Chaari F, Markiewicz E, et al. (2009) Micromechanical modeling of the anisotropy of elastic biological composites. *Multiscale Modeling and Simulation* 8(1): 326–336.
Saanouni K and César de Sa JMA (2011) Advances in continuum damage mechanics. *International Journal of Damage Mechanics* 20(04): 483.
Schonning A, Oommen B, Ionescu I, et al. (2009) Hexahedral mesh development of free-form formed geometry: The human femur exemplified. *Computer-Aided Design* 41: 566–572.
Shen WQ, Lin J, Zhu QZ, et al. (2011) Macroscopic yield criterion for ductile materials containing randomly oriented spheroidal cavities. *International Journal of Damage Mechanics* 20(08): 1198–1216.
Siris ES, Chen YT, Abbott TA, et al. (2004) Bone mineral density thresholds for pharmacological intervention to prevent fractures. *Archives of Internal Medicine* 164(10): 1108–1112.
Voyiadjis GZ, Kattan PI and Taqieddin ZN (2007) Continuum approach to damage mechanics of composite materials with fabric tensors. *International Journal of Damage Mechanics* 16(3): 301–329.
Yoshida H, Faust A, Wilckens J, et al. (2006) Three-dimensional dynamic hip contact area and pressure distribution during activities of daily living. *Journal of Biomechanics* 39(11): 1996–2004.
Zhang J and Zhang X (2003) A robust SQP method for optimization with inequality constraints. *Journal of Computational Mathematics* 21(2): 247–256.